

Detection of Lithium-Ion Cells' Degradation through Deconvolution of Electrochemical Impedance Spectroscopy with Distribution of Relaxation Time

Pietro Iurilli,* Claudio Brivio, and Vanessa Wood


Herein, a methodology to investigate aging of commercial cylindrical Li-ion cells is introduced. Distribution of relaxation time (DRT) method is applied to deconvolute electrochemical impedance spectroscopy (EIS) measurements and separate those polarization effects that are usually overlapped in the frequency domain by means of a peak-based representation. Half-cells are built at the beginning and end of life to link the electrochemical and aging processes occurring at anode and/or the cathode sides. Moreover, lab-made full-cells are exploited to verify the reproducibility when compared with cylindrical cells. The results of an extensive analysis of around 500 EIS spectra return an unambiguous attribution of different electrochemical processes to different time constants and ultimately to different DRT peaks. Digital imaging validates graphite degradation, mainly related to lithium plating. Scanning electron microscopy validates the degradation at NMC cathode, mainly attributed to particle cracking. It is concluded that DRT peaks allow to characterize cell aging and their tracking can help to develop more reliable state of health estimators.

1. Introduction

Nowadays, Li-ion batteries are widely used in stationary energy storage, electric vehicles, and consumer electronics, thanks to their ideal performances in terms of energy and power densities.^[1,2] However, their aging is still a big uncertainty being caused by complex physical and chemical degradation mechanisms which affect the different components inside the cell.^[3,4] These mechanisms do not leave a unique fingerprint

P. Iurilli, C. Brivio
Sustainable Energy Center
CSEM
2002 Neuchâtel, Switzerland
E-mail: pietro.iurilli@csem.ch

P. Iurilli, V. Wood
Department of Information Technology and Electrical Engineering
ETH Zürich
8092 Zürich, Switzerland

 The ORCID identification number(s) for the author(s) of this article can be found under <https://doi.org/10.1002/ente.202200547>.

© 2022 The Authors. Energy Technology published by Wiley-VCH GmbH. This is an open access article under the terms of the Creative Commons Attribution-NonCommercial-NoDerivs License, which permits use and distribution in any medium, provided the original work is properly cited, the use is non-commercial and no modifications or adaptations are made.

DOI: 10.1002/ente.202200547

on the cell characteristics but they can be clustered into the so-called degradation modes: 1) loss of lithium inventory, which entails the consumption of lithium ions for decomposition reactions, solid–electrolyte interface (SEI) layer growth, or lithium plating; 2) loss of anode active material, and 3) loss of cathode active material, which both encompass electrode structural disordering, particle cracking, and loss of electric contact.^[5] Therefore battery cell measurements should be comprehensive, to embrace the complex interactions between the degradation modes, and non-invasive, to be implemented in battery management systems (BMSs) and ultimately provide a correct estimation of the state of health (SoH)—the remaining capacity with respect to the original one.^[2,6,7] Electrochemical impedance spectroscopy (EIS) is an example of a comprehensive measurement widely used to characterize Li-ion cells.^[8–11] In literature, several works applied EIS to investigate and track Li-ion cells' aging: a summary of those applications and of the best metrological practices is given in our previous work and in the works of Choi et al. and Meddings et al.^[12–14] In general, the impedance spectrum of a cell is analyzed and fit with an electric circuit model (ECM) to extract the parameters related to the single electrochemical processes occurring inside the cell.^[11,15,16] However, given the complexity to separate these processes in the EIS spectra, the distribution of relaxation time (DRT) is often used to deconvolute the impedance curves in the time domain and distinguish polarization effects that are normally overlapped in the frequency domain.^[17,18] These polarization effects are characterized by peaks with different magnitudes and time constants that can be attributed to the underlying physical processes.^[19] For instance, Yi et al. applied DRT to investigate the aging of cells in different conditions.^[20] The authors developed a support vector machine classifier to analyze the DRT peak variations caused by lithium plating with respect to cell beginning of life (BoL). A similar work is presented by Zhou et al., characterizing NMC pouch cells under high-temperature cycling.^[21] The authors decoupled the degradation mechanisms of the anode from the ones on the cathode by focusing on different DRT peaks. However, they concluded that a further step was required to confirm the assumptions made. Including a reference electrode in the cell or manufacturing half-cells with the same material of the full-cells and lithium metal as counterelectrode is the solution normally

adopted in literature.^[22,23] In this way, electrochemical characterizations (i.e., EIS measurements) are done separately on the anode half-cell and cathode half-cell and reconciled with the full-cells for validation purposes. Wildfeuer et al. made half-cells from commercial NCA cylindrical cells and performed DRT characterization on them at different temperatures and state of charges (SoCs).^[24] They concluded that charge transfer processes on the full-cell are dominated by the cathode at low SoC and by the anode at high SoC. Moreover, they found that a transition process between charge transfer and solid-state diffusion might be attributed to the anode. Sabet et al. characterized both NCA cylindrical and NMC pouch cells.^[25,26] They attributed the two main DRT peaks to the SEI layer and cathode charge transfer for both the cell chemistries. These insights were also exploited in a following publication, to investigate accelerated aging of NMC cells.^[2] The authors attributed the two DRT peak variations 1) to SEI growth and 2) to cathode particle cracking, cathode–electrolyte interface (CEI) growth, and cathode dissolution. These conclusions were validated by means of postmortem analyses, which is the most widely used process to validate electrochemical findings. Postmortem analyses allow to investigate the chemical structure and surface morphology of the electrodes, providing valuable and detailed information about the chemical composition and degradation.^[27,28] For an exhaustive summary of all the available techniques, their advantages, and limits, the readers are addressed to the review article of Waldmann et al.^[29] A simple implementation of imaging techniques combined with half-cell DRT analysis is given by Chen et al. who studied lithium plating of LCO pouch cells.^[30] The authors built symmetrical lithium metal cells to address the influence of the reference electrode on the DRT profiles of half-cells. They overdischarged anode half-cells to simulate the existence of different amounts of lithium plating and highlight its effect on the DRT profile. Then, they analyzed the results of cycling aging tests of cylindrical cells at 0 °C. Based on their measurements, the authors attributed the variations of DRT peaks during aging mainly to the anode electrode. Similar conclusions, on the importance of the anode in cells' aging, were drawn by Heins et al., who studied large-format NMC pouch cells at different temperatures.^[31] The authors exploited a three-electrode configuration to deconvolute the effects of the two electrodes but did not perform further analyses to assess the degradation mechanisms.

Overall, EIS is a comprehensive measurement and DRT is a promising postprocessing method to analyze cell aging and to detect the influence of different degradation mechanisms.

However, there are two main limitations found in the literature. 1) DRT is applied either at BoL, that is, with no aging, or analyzing a specific degradation mechanism, neglecting other effects.^[20,24,30] 2) DRT peak attribution is not performed univocally, either based on existing literature or validating the result with half-cells and postmortem analyses only for the most relevant peaks and not for the full time constant range.^[21,25,31]

Therefore, the objective of this work is to overcome those limits with an exhaustive methodology that systematically analyzes DRT profiles and, by means of a validation process, unambiguously attributes DRT peaks to the degradation mechanisms arising during cell aging. Commercial cylindrical cells are cycled in different testing conditions to embrace different degradation mechanisms. EIS measurements are taken from cylindrical cells and from lab-made full-cells and half-cells containing the material harvested from the cylindrical cells. The obtained DRT profiles are analyzed at BoL, to link physical processes to specific peaks, and at EoL, to link aging effects to the same peaks. Imaging techniques with different accuracy, complexity, and duration are exploited to characterize the surface morphology of the electrodes and validate the earlier attributions between DRT peaks and degradation mechanisms. Three techniques have been selected: digital imaging, optical microscopy, and SEM.

The article is structured as follows. Section 2 presents the developed methodology, which includes all the steps necessary to fully investigate Li-ion cells with EIS measurements and DRT postprocessing. Section 3 presents the main findings derived from the performed aging tests, which include the attribution of DRT peaks to electrochemical processes at BoL, the attribution of aging phenomena at EoL, and their validation through imaging techniques. Finally, Section 4 summarizes the main takeaways from the authors.

2. Experimental Section

The findings of this work were based on testing cylindrical commercial Li-ion cells: LG chem INR21700-M50 with lithium nickel manganese cobalt oxide cathode (NMC 811) and graphite with silica particles anode (graphite–SiO_x).^[32] First, all the cells were checked in their capacity and impedance values to ensure the reproducibility of the results. Second, all the cells were subjected to the same testing campaign following the methodology shown in **Figure 1**: 1-a) the cells were cycled with different testing protocols from BoL till EoL, which was defined for SoH lower than

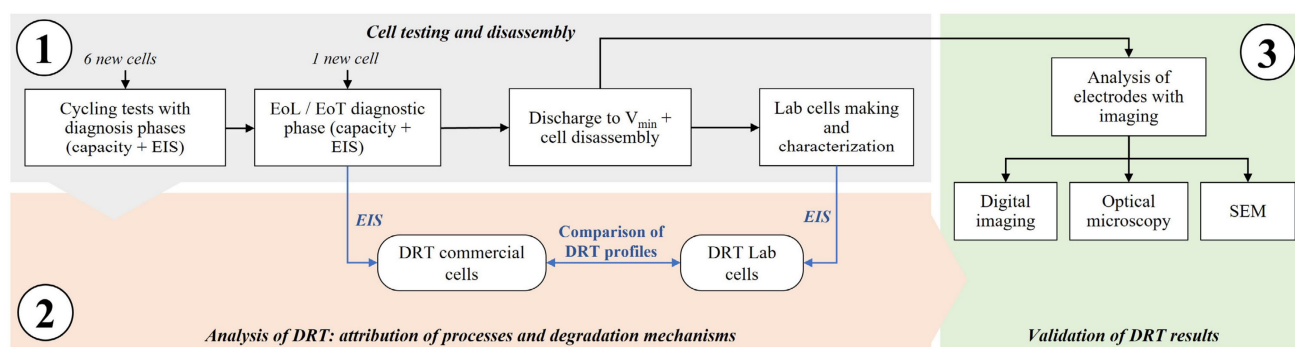


Figure 1. Methodology followed in this work: testing, analysis/attribution, and validation.

80% or End of Test (EoT), which was fixed to 1000 equivalent cycles (EqC) (Equivalent cycle: it is defined as the ratio between the cumulated cycled capacity of a cell and two times its nominal (or initial) capacity.). EIS measurements were done at regular intervals to update the impedance; 1-b) the cells were discharged and disassembled to extract the electrode material, which was used to assemble coin cells and to run imaging for postmortem analyses. 2) The EIS/DRT measurements from both commercial and half-cells, pristine and aged, were analyzed to attribute electrochemical processes and assign degradation mechanisms to the anode or the cathode. 3) Imaging was used to validate the correctness of the attribution, specifically digital imaging, optical imaging, and SEM. In total 7 cells were investigated in this work and the performed experiments are presented in **Table 1**. The next paragraphs will provide more information about testing and disassembly, analysis of DRT profiles, and validation with imaging techniques.

2.1. Cell Testing and Disassembly

The experiments were performed at the CSEM's Sustainable Energy Center, Neuchâtel (Switzerland). The first part of the presented methodology is divided in three steps: cycling aging tests, cell disassembly, and lab-cell making.

2.1.1. Cycling Aging Tests

The testing setup was composed of: 1) a cell tester Biologic BCS815 equipped with 32 parallel, 9 V–15 A channels ($\pm 0.01\%$ full-scale deflection [FSD] accuracy on the voltage and $\pm 0.015\%$ FSD accuracy on current, for each available range) with an EIS spectroscope multiplexed and able to range from 10 kHz to 10 mHz^[33] and 2) a thermostatic chamber ATT-DM1200T with $-45\text{ }^{\circ}\text{C}$ – $180\text{ }^{\circ}\text{C}$ temperature range.^[34] The temperature during the experiments was fixed to $20\text{ }^{\circ}\text{C}$. As anticipated, the seven cells were first characterized with capacity tests and EISs to ensure the

reproducibility of the results. Capacity test showed a standard deviation of 0.5% with respect to the cells' averaged capacity. EIS spectra showed a standard deviation of 1.0% on the ohmic resistance (i.e., the zero-crossing value on the EIS Nyquist plot) and 3.3% on the polarization resistance (i.e., the full resistivity down to 10 mHz) with respect to the averaged values.

Different testing conditions were set which differed in the current rates (C-rate) and the depth of discharges (DoD) applied during the cycling phase. The testing conditions are listed in Table 1, with the corresponding cell ID. The reference cell (ID:REF) followed the cycling conditions as defined by the manufacturer (C/3 both in charge and discharge). Another cell was cycled in the reference condition but without the constant voltage (CV) phase (ID:REF_w/oCV). The remaining cells were cycled with higher C-rates and/or smaller DoD to explore different aging conditions and spot different degradation mechanisms.

Regardless from the specific cycling conditions, all experiments alternated cycling phases of 50 EqC and diagnostic phases. The diagnostic phase included capacity determination (i.e., SoH measurement) in nominal conditions and EIS characterization at five SoC levels: 0%:25%:100%. In this way, the impedance evolution of each cell was tracked during its lifetime and it was possible to compare cells with different cycling conditions. The SoC levels were fixed to a specific voltage value extracted by the cells' open-circuit voltage (OCV) curve at BoL; those values remained unchanged throughout the test duration. The last diagnostic phase was performed at EoL/EoT condition before cell disassembly.

2.1.2. Cell Disassembly

Cell disassembly procedure was developed and optimized based on the existing literature.^[10,23,25,26,35–38] First, the cell was discharged to the minimum voltage (i.e., 2.5 V) at C/3 constant rate and a CV phase with cutoff current of C/100. After that, the cell was transferred inside an argon-filled glovebox. A pipe cutter was

Table 1. Overview of the cycling protocol applied to the different tested cells. Legend: "✓" test performed; "✗" test not performed; "A" anode; "C" cathode.

Testing protocols					Postmortem analyses		Imaging techniques		
Cell ID	DoD	SoC interval	Charging rate	Discharging rate	Cell disassembly	Lab-cell making	Digital imaging	Optical microscopy	SEM
NEW	–	–	–	–	✓	✓	C: ✓ A: ✓	C: ✓ A: ✓	C: ✓ A: ✓
REF	100%	0%-100%	C/3 ^{a)}	C/3	✓	✓	C: ✓ A: ✓	C: ✓ A: ✓	C: ✓ A: ✓
REF_w/oCV	100%	0%-100%	C/3	C/3	✓	✓	C: ✓ A: ✓	C: ✗ A: ✓	C: ✗ A: ✗
DOD20	20%	0%-20%	C/3	C/3	✓	✓	C: ✓ A: ✓	C: ✗ A: ✓	C: ✗ A: ✓
FC05	100%	0%-100%	C/2 ^{a)}	C/3	✓	✓	C: ✓ A: ✓	C: ✗ A: ✓	C: ✗ A: ✗
FC1	100%	0%-100%	1C ^{a)}	C/3	✓	✓	C: ✓ A: ✓	C: ✓ A: ✓	C: ✓ A: ✓
FD1	100%	0%-100%	C/3 ^{a)}	1C	✓	✓	C: ✓ A: ✓	C: ✗ A: ✓	C: ✗ A: ✗

^{a)}Including CV phase with cutoff current at C/50.

used to open the cell on the bottom and on the top sides and the electrodes tabs were cut; the lateral part of the case was removed using pliers. A scalpel was used to cut the tape that closes the jellyroll (i.e., electrodes + separator foils) and the cell components were unrolled and separated. References of the inward and outward facing side as well as of the outer and inner roll part of the electrodes were taken to properly reuse the material in the following steps. The electrodes were not washed with DMC to preserve their aged state and properly perform electrochemical measurements.^[29,39] The electrodes were cut following a precise procedure to guarantee consistency between the different cells analyzed: 1) adjacent parts of the outer roll of the electrodes were cut for lab-cell making and for imaging techniques' application; 2) the electrodes were fixed on a hard substrate with adhesive tape; 3) coating on one side of the double-coated electrodes was removed using NMP solvent for both the cathode and anode material for practical reasons; and^[32,39] 4) the foils were punched in a central area (i.e., equidistant from the edges) to obtain 15 mm-diameter disk electrodes.

2.1.3. Laboratory Cells' Making

Lab cells were made in 2025 coin format, including two 0.5 mm aluminum spacers (at top and bottom) and glass fiber separator Whatman GF/C with 19 mm diameter. The standard electrolyte was 1 M lithium hexafluorophosphate (LiPF₆) in a mixture of ethylene carbonate, dimethyl carbonate, and diethyl carbonate produced by Sigma-Aldrich (EC:DMC:DEC, 1:1:1 w/w/w) with a quantity of 90 μL. Three types of coin cells were made with the electrodes extracted by the cylindrical cells. 1) Full-cells: Graphite and NMC were coupled to reproduce the standard cylindrical cell and assess the possible differences due to cell making process or new electrolyte. 2) Anode half-cells: Graphite was coupled with a disk of lithium metal (reference electrode). 3) Cathode half-cells: NMC was coupled with a disk of lithium metal.

Three identical samples were built for each cell type, with a total number of 9 cells, to reduce risks of nonreproducibility due to assembling process. Cell formation was performed with two cycles at C/10 after 12 h rest to allow the electrolyte to soak the electrodes and the separator.^[38] The voltage range was 3–4.2 V for full and cathode half-cells and 0.01–1 V for anode half-cells. After formation, the cells were characterized with EIS measurements at voltages corresponding to 0%, 50%, and 100% SoC of the full-cell SoC. The specific voltage values were chosen performing the OCV curves' balancing of the half-cells and of the full-cell as presented in literature.^[40] EIS measurements were used to verify cells reproducibility and to discard the cells with abnormal impedance with respect to their twin samples. The standard deviation showed a value of 13.6% for the polarization resistance with respect to its averaged value. However, it reduced to 5.3% when evaluated down to 0.1 Hz only, that is, in the most interesting portion of the spectra for DRT peak attribution. It was therefore concluded that the EIS spectra of lab-made cells were of similar quality with respect to the ones of commercial cells, thus confirming the reliability of the assembly process.

2.2. Analysis of DRT Profiles

All EIS measurements were checked in their quality and time invariance with the Kramers–Kronig (KK) criterion, which returned the residual between the measured spectra and reconstructed KK spectra.^[41,42] If the criterion was respected, the DRT function could be computed as follows.

$$Z(j\omega) = R_{\text{ohmic}} + \int_0^{\infty} \frac{g(\tau)}{1 + j\omega\tau} d\tau \quad (1)$$

The DRT calculation was based on the assumption that an impedance spectrum could be represented as an infinite series of RC elements and the ohmic resistance. The $g(\tau)$ function was discretized and solved applying regularization methods; details about the mathematical formulation are given in literature by Wan et al.^[43] All the algorithmic steps to compute DRT from EIS for Li-ion cells were presented in a previous work from the same authors of this manuscript.^[18] $g(\tau)$ function had a peak-based representation, as shown in Figure 2; specific letter and number were used to define the origin and the peak position. The letters used were “S” for cylindrical cells (i.e., the standard cells), “F” for laboratory full-cells, “C” for cathode half-cells, and “A” for anode half-cells (e.g., Figure 2 represents the DRT profile at BoL and 50% SoC for a cylindrical cell). As introduced in Section 1, each peak could be attributed to a different process occurring in the cell. For this reason, high-quality and time-invariant EIS measurements are required; otherwise, the $g(\tau)$ function will show artefacts and the peak attribution will not be reliable.

Three criteria were defined to evaluate which specific phenomenon could be attributed to which one of the electrodes and ultimately to which degradation mechanism. Those criteria are used twofold: 1) to compare DRT measured on lab-made full-cells with lab-made half-cells' full-cell and 2) to compare the same between lab-made full-cells and cylindrical cells. While the first was used to discriminate between the processes at the cathode or at the anode sides, the second served to verify the consistency in the measurements between the cylindrical cells and lab cells. The chosen criteria were as follows. 1) Time constant (τ): Depending on the value of the time constant, a specific peak can be attributed to a defined physical process. The four main

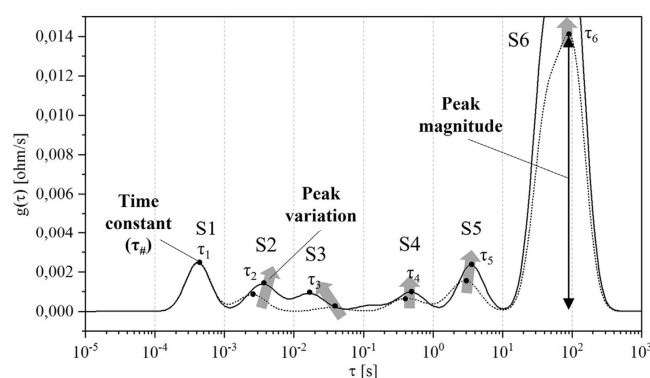


Figure 2. Typical DRT profile of a Li-ion cell and the criteria used to evaluate DRT peaks: time constant, peak magnitude, and peak variation.

processes that can be allocated were 1) electric and magnetic effects ($\tau < \approx 10^{-3}$ s); 2) transport of lithium ions through the SEI or CEI layers ($\approx 10^{-4} < \tau < \approx 10^{-2}$ s); 3) electrodes' charge transfer ($\approx 10^{-2} < \tau < \approx 10^1$ s); and 4) diffusive processes ($\tau > \approx 10^1$ s).^[2,21,30,35,42,44] 1) Peak magnitude: The peak magnitude was calculated by measuring the height of the peak, as shown in Figure 2. This indicator is mainly used to compare the peaks of lab cells (full or half-cells). 2) Peak variation with respect to SoX: The peak variation was evaluated with respect to SoC (i.e., different OCVs) and to SoH (i.e., different aging stages). In both cases, the indicator allows to understand which electrode mainly affects the DRT peak behaviors.

2.3. Validation of DRT Results

The DRT peak attributions defined through the presented criteria were validated via imaging techniques. Three types of imaging with increasing precision, complexity, and operation time were performed: 1) digital imaging by means of a nonprofessional camera, 2) optical microscopy by means of an Olympus BX53M, and 3) SEM by means of a Thermo Scientific Scios. Digital imaging was performed by taking pictures of the unrolled electrodes, to detect macroeffects on the surface, such as defects, plating, or material exfoliation.^[26,45] Optical microscopy was used to detect degradation mechanisms in the micrometer range, such as cracks in electrode coating, growth of films on the electrode surface, delamination, or decomposition of electrodes.^[29] Finally, SEM was performed to investigate the surface morphology and electrode microstructure, allowing to relate their changes to degradation mechanisms, such as particle cracking or changes/film formation on particle surface.^[28,46–48] Both surface (planar samples) and cross-section samples were analyzed.

The validation process was performed by connecting the results obtained by imaging with the results of tentative peak attributions for lab cells (half and full-cells) and cylindrical cells. For instance, if cathode imaging reveals particle cracking and the analysis of cathode half-cell reveals a relevant rise of peak C4 with respect to BoL value, then this peak is attributed to cathode particle cracking. Similar conclusions are done if anode imaging reveals lithium plating and anode half-cell DRT analysis shows a large rise of peak A2. The validation of full-cells and cylindrical cells was performed by combining the results obtained from anode and cathode analyses. However, given the different detection capabilities of the presented imaging techniques, the validation process could be limited by the precision of the available equipment in the testing facility where measurements were performed.

3. Results and Discussion

The cells have been cycled with different testing protocols as already presented in Table 1. Overall, the testing results are presented in **Figure 3**, with the SoH progression and EqC for the six cycled cells (cell ID:NEW was disassembled at BoL, i.e., SoH = 100%). The cell cycled in reference condition (ID:REF) reached the EoT (testing limit of 1000 EqC) at SoH = 86%. Increasing the C-rate is detrimental for battery performances. Higher charging rates are more severe than higher discharging rates: cell FC1 and cell FC05 reach their EoL (SoH = 80%) after

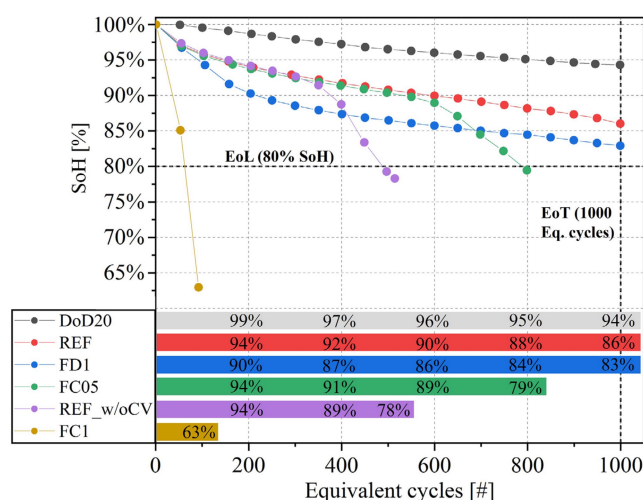


Figure 3. SoH versus EqC for the six cycled cells. Tests were stopped once EoL (SoH = 80%) or EoT (equivalent cycles = 1000) conditions were met.

92 and 798 EqC, while cell FD1 reached SoH = 81% at the EoT. Reduction of the DoD (i.e., of the voltage range available for cycling) brought less-severe cell aging: SoH = 94% at EoT for cell DOD20. Finally, the cell REF_w/oCV shows an unexpected trend: only 500 cycles at EoL but with a cycling protocol lighter than cell REF. This is most probably due to an early-stage slope change (the so-called “knee”), which can be attributed to film formation on the electrode surface, such as early lithium plating deposition caused by production defects (electrode surface defects or electrolyte quantity) and not detectable at BoL.^[49]

3.1. Analysis of DRT Profiles

The DRT profiles of cylindrical cells were derived from the EIS performed every 50 EqC. On average for the tested cells, the maximum residuals between the measurement and KK reconstruction were lower than 1.1% at BoL and lower than 1.0% at EoL/EoT, allowing for a reliable DRT calculation. **Figure 4** shows an example of DRT profile evolution at SoC = 50% (the peak S6 was omitted to better appreciate the changes on the smaller peaks). In most of the cases, peaks S2, S3, and S4 show the most relevant trend at increasing cycle numbers with a clear link to the SoH decrease: for instance, the steepest the capacity fade, the highest the growth of peak S2.

In the following paragraphs, the criteria explained in Section 2.2 (time constant, peak magnitude, peak variation) will be applied to lab-cells and cylindrical cells' DRT profiles at both BoL and EoL/EoT. The first serves to discuss which electrochemical process should be associated with which DRT peak and the second serves to identify which peak should be tracked to identify which degradation mechanism.

It is worth to mention that for half-cells the presence of the reference electrode (i.e., lithium metal) influences the impedance response and consequently the DRT profile of the cells.^[30] Symmetric lithium metal cells have been produced to verify that DRT profiles show one main peak with time constant around 6×10^{-4} s.

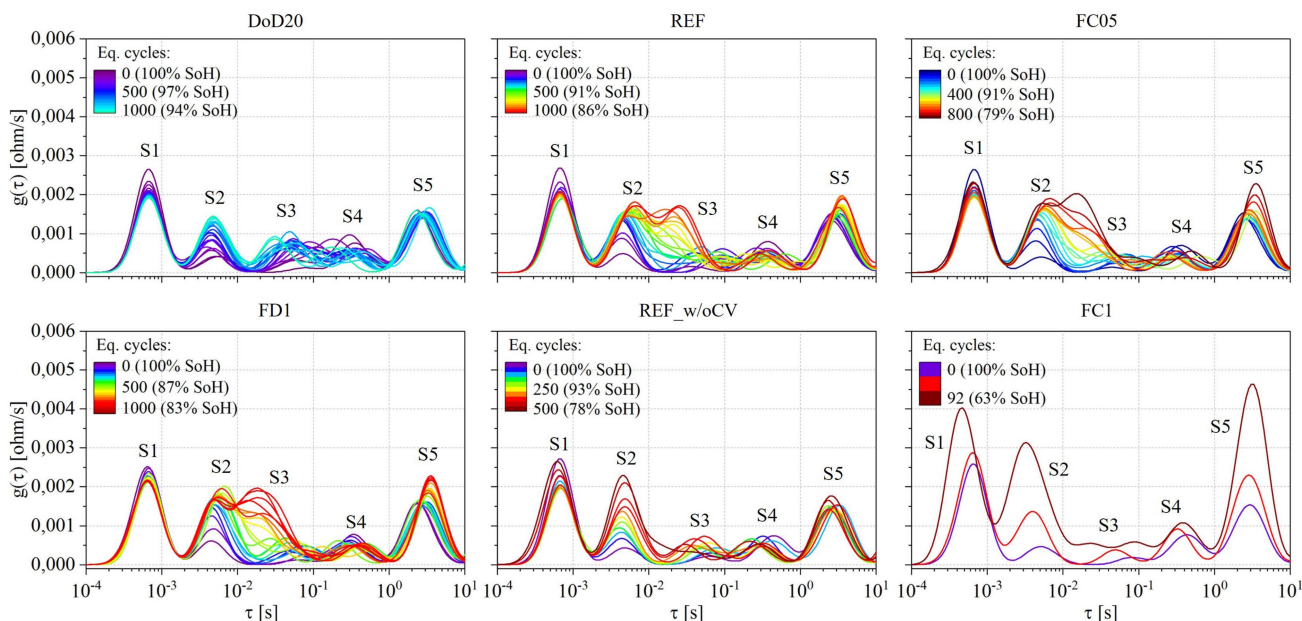


Figure 4. 50% SoC DRT profiles trends during cycling of the six tested cells. The color scale is based on the SoH (violet = 100% SoH; brown \leq 80% SoH).

3.1.1. Assessment at BoL

The first cell that has been disassembled is the ID:NEW (SoH = 100%). **Figure 5** shows the DRT profiles at different SoCs including the results of lab cells (anode, cathode half-cells,

and full-cells). The slight time constants shifts at values lower than 10^{-2} s between cylindrical cell and lab cells are mainly given by differences in the fabrication procedure due to cell format and cell components. As regards cell format, coin cells are free from inductive behavior, so the first peak time constant is

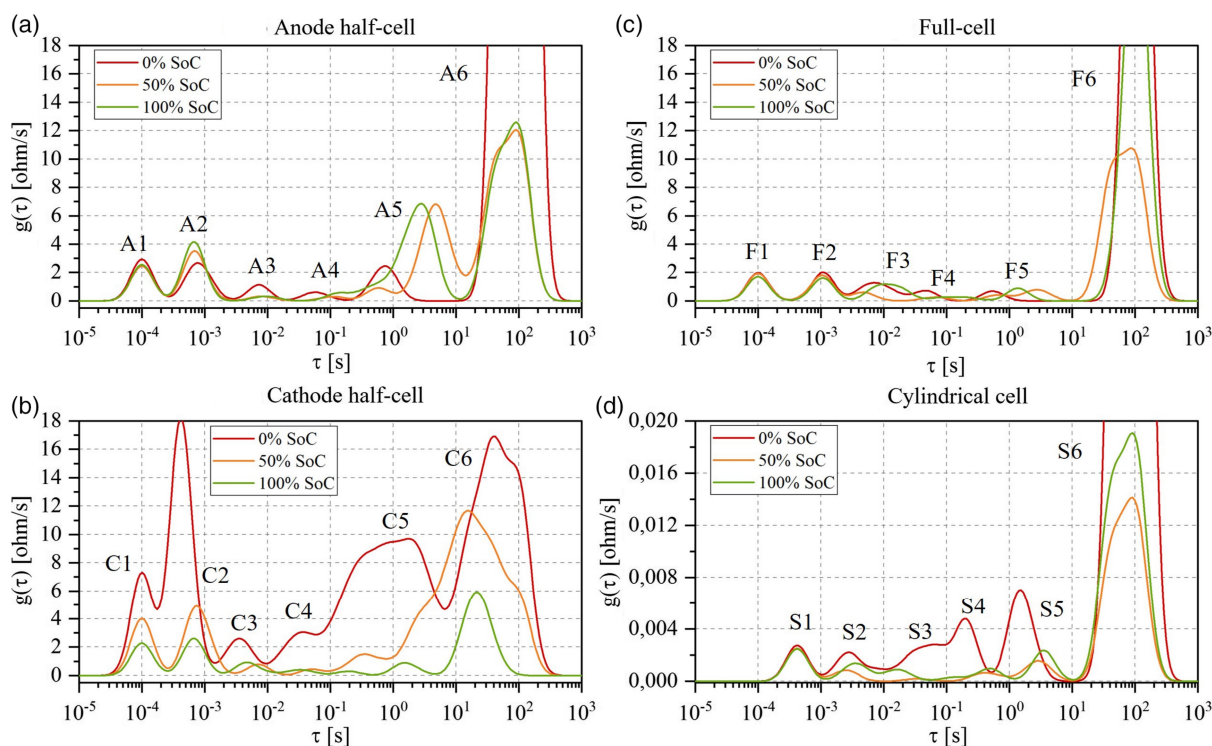


Figure 5. DRT profiles at 0%, 50%, and 100% SoC of cell NEW (BoL). a) Anode half-cell; b) cathode half-cell; c) full-cell (coin format); and d) cylindrical cell.

shifted to lower values with respect to cylindrical cells, around 10^{-4} s.^[24,30] As regards cell components, lab-made cells will be always slightly different from the original dismantled cells due to the different separator and electrolyte additives.^[35]

The criteria defined in Section 2.2 have been applied: 1) to compare the DRT profiles of anode half-cell (Figure 5a) and cathode half-cell (Figure 5b) with respect to the full-cell ones (Figure 5c) and 2) to compare the DRT profiles of the full-cell with respect to the cylindrical cell ones (Figure 5d). The analysis is performed peak by peak, from 1 to 6, by referring to the nomenclature previously introduced: “S” for cylindrical cells (i.e., the standard cells), “F” for laboratory full-cells, “C” for cathode half-cells, and “A” for anode half-cells. 1) Peak 1: Half-cells (A1, C1) and full-cells (F1) have the same time constant ($\tau = 10^{-4}$ s) but slightly different behavior with respect to SoC: peaks A1 and F1 have similar magnitude and are invariant across SoCs; peak C1, instead, shows an increasing magnitude for lower SoC. The behavior of C1 could be influenced by the large magnitude of peak C2, especially at 0% SoC. In literature, electric and magnetic effects due to particle–particle and particle–current collector interactions are usually attributed in this time constant range.^[21,30,42] Therefore, peaks A1, C1, and F1 are also linked to these effects. The same phenomenon is also observed in the cylindrical cell with S1 but at a slightly lower time constant. 2) Peak 2: Half-cells A2 and C2 have similar time constants values ($\approx 7 \times 10^{-4}$ s) while F2 has a slightly bigger one (10^{-3} s). The DRT peaks are influenced by the presence of the lithium metal reference electrode in the half-cells: this phenomenon is especially observed in the cathode one where large magnitude variations at low SoC are registered.^[30] Peak A2 instead shows smaller variations with respect to SoC and, given its time constant, is also influenced by the transport of ions in graphite’s SEI layer, as described in the literature.^[21,30] Therefore, by comparison of peak magnitudes and knowing that lithium metal is not included in full-cells, peak F2 is tentatively attributed to graphite’s SEI layer. Analogously, peak S2 (cylindrical cell) is attributed to the same phenomena. 3) Peak 3: At the cathode side, peak C3 shows the lowest magnitude and the smallest change with SoCs if compared with all other peaks. The time constant is between 3×10^{-3} and 7×10^{-3} s at which CEI formation is typically attributed in the literature.^[25,26] At the anode side, half-cell peak A3 has a time constant close to 10^{-2} s, in a region where interface and charge transfer effects could be overlapped.^[26,30,42,50] By looking at the peak magnitude variations with respect to SoC, A3 shows a behavior typically depicted for the charge transfer process and similar to peak A4 rather than peaks A2 or C2 that are related to SEI layer and lithium metal reference electrode, respectively.^[42] Therefore, peak A3 is attributed to graphite charge transfer. When comparing half-cells with the full-cell, F3 is tentatively attributed to the cathode, due to its larger magnitude both at SoC = 0% and at SoC = 100%, which are typically related to the cathode.^[24,30] When analyzing the cylindrical cell, S3 shows differences (e.g., SoC trend) if compared with F3 but similarities if compared with C4. Therefore, S3 is tentatively attributed to the cathode. 4) Peak 4: At the anode side, peak A4 shows a very similar behavior to A3 but time constant around 10^{-1} s; therefore, it is attributed to graphite charge transfer processes. At the cathode side, charge transfer processes are usually marked by peaks with broad magnitude

variations with respect to SoC, in the time constant interval 10^{-2} – 10^1 s.^[24,26] Given the match found on the cathode half-cell, C4 is attributed to NMC charge transfer reactions. When analyzing the full-cell, peak F4 cannot be clearly attributed to the anode nor the cathode. Moving then to the cylindrical cell, S4 shows large magnitude variations with SoC, as observed for NMC charge transfer. Peak S4 is therefore tentatively attributed to NMC charge transfer. 5) Peak 5: At the anode side, peak A5 shows small magnitude and time constant (8×10^{-1} s) at SoC = 0% followed by magnitude growth and a time constant shift to larger values at SoC = 50% and SoC = 100%. This peak is attributed to charge transfer processes, as found in the literature.^[24,42] At the cathode side, peak C5 is characterized by a wide SoC variation and therefore attributed to NMC charge transfer, similar to peak C4. Moreover, peak C4 and C5 are partially overlapped at SoC = 0% SoC. Same behavior is also found in the full-cell and cylindrical cells with peaks F3/F4 and S3/S4, respectively. If peak F4 is tentatively attributed to NMC charge transfer, peak F5, which shows the same time constant shift and SoC variations as in peak A5, is instead attributed to graphite charge transfer. The same conclusion applies for the fifth peak in the cylindrical cell (S5). 6) Peak 6: This peak shows the largest magnitude and variations with respect to SoC both for lab cells and the cylindrical cell. Given the time constant higher than 10s, this peak is attributed to diffusive processes.^[42] When comparing the behaviors of peaks A6/C6 with respect to F6, it is hard to define which electrode has the biggest impact on the full-cell. Consequently, peak F6 and analogously S6 are attributed to the diffusive processes occurring at both electrodes.

The summary of DRT analysis at BoL for half-cells, full-cells, and cylindrical cell is given in **Table 2** with the tentative attribution of physical processes to each DRT peak. The analysis at EoL/EoT and imaging techniques will be used to refine and unambiguously validate these results.

3.1.2. Assessment at EoL/EoT

The assessment at EoL/EoT is done by comparing the DRT profiles of cells that performed cycling tests with the pristine ones (ID:NEW) presented in the previous paragraph. **Figure 6** shows the results at 50% SoC for half-cells, full-cells, and cylindrical cells for different SoH values. As in the previous paragraph, the peak analysis is performed from peak 1 to peak 6. 1) Peak 1: This peak does not have a clear trend with respect to cells’ SoH both in lab-made cells and in cylindrical cells. In the first case, the small variability on the magnitude is attributed to the cells’ assembling process. In the second case, the larger magnitude is observed for cell ID:FC1 that was severely aged (63% SoH). However, no clear behavior linked to cycling is found and the attribution to electric and magnetic effects is confirmed with no specific link to any degradation. 2) Peak 2: Anode and cathode half-cells show similar magnitudes (peak heights) for peaks A2 and C2 but not related to SoH levels. More in detail, C2 shows a significant higher magnitude for cells ID:NEW (100% SoH) and ID:DOD20 (94% SoH) than for all the other cells. This trend is unrelated to material degradation and is referred to impurities of lithium metal electrode surface. In the case of A2, the peak variability can be addressed to differences among the cells in the SEI

Table 2. Tentative DRT peaks' attribution at BoL.

	Electric and magnetic effects	SEI film	Li metal reference electrode	CEI	Cathode charge transfer	Anode charge transfer	Diffusion processes
Anode half-cell	A1	A2	A2	–	–	A3, A4, A5	A6
Cathode half-cell	C1	–	C2	C3	C4, C5	–	C6
Full-cell	F1	F2	–	–	F3, F4	F5	F6
Cylindrical cell	S1	S2	–	–	S3, S4	S5	S6

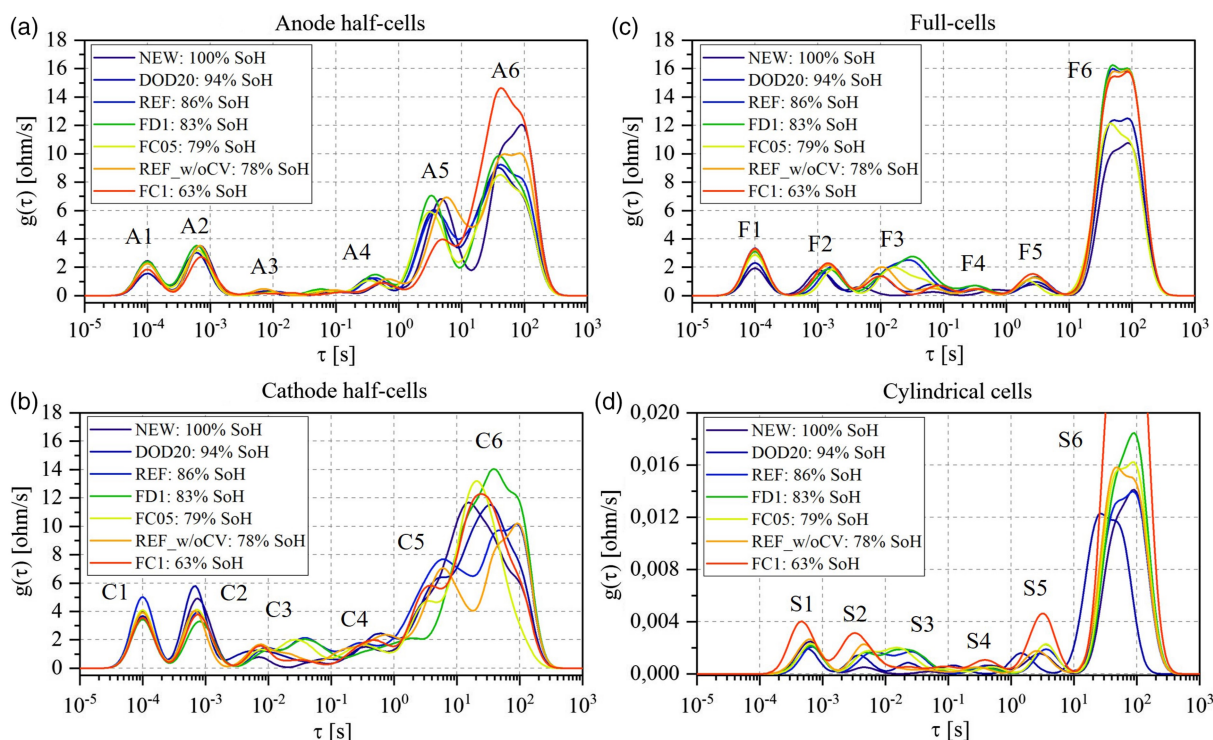


Figure 6. DRT profiles at 50% SoC of a cell NEW (100% SoH) and of the tested cells at EoL/EoT: a) anode half-cells; b) cathode half-cells; c) full-cells (coin format); and d) cylindrical cells.

layer. It is worthwhile to mention that larger variations were expected for this peak related to SEI growth/decomposition and surface film formation (lithium plating). However, for consistency in the postmortem procedure, the disk electrode for coin cells was always cut in the same area on the outer side of graphite that, in most the cases, was not severely aged as the inner part. If compared with the half-cells, peaks F2 show lower magnitude but increasing trend at decreasing SoH. Knowing that C2 is mostly influenced by lithium metal electrode, F2 is tentatively attributed to the SEI peak (A2), confirming BoL analysis. This is also true in the cylindrical cell (S2), especially for cells that reached SoH < 80% before 800 EqC (ID:FC1, REF_w/oCV, and FC05). Therefore, peaks F2 and S2 are tentatively attributed to the SEI layer growth/decomposition. However, given the great variations in S2, this peak is also tentatively linked to lithium plating. 3) Peak 3: At the anode side, peak A3 does not show relevant variations with SoH. At the cathode side, peak C3 shows two trends: 1) moderate rise in magnitude with no time constant

variations for cells ID:FC1, ID:REF_w/oCV, and ID:DOD20 and 2) large rise in magnitude and shift toward bigger time constants for cells ID:FC05, ID:FD1, and ID:REF. Therefore, cathode degradation looks more relevant after a certain number of cycles (i.e., 700 EqC) and at certain SoH (e.g., SoH < 94%). Similar peak behaviors are found analyzing F3 and S3 that confirm the attribution at BoL and that are consequently attributed to NMC degradation mechanisms (such as particle disordering and cracking). 1) Peak 4: Peaks A4 and C4 show a rise in magnitude for cycled cells compared with cell ID:NEW. In both cases, this phenomenon is attributed to electrode degradation which affects charge transfer processes. When analyzing F4 and S4, peak variations are less pronounced but show similar trends. Therefore, and coherently with respect to peak 4 attribution at BoL, peaks F4 and S4 are tentatively attributed to cathode degradation. Imaging techniques applied on electrode material will be used to validate this result. 2) Peak 5: No specific trend with SoH is found at the anode side, nor at the cathode side. However, when

Table 3. Tentative DRT peak attribution at EoL/EoT.

	SEI growth/ decomposition	Lithium plating	Cathode degradation	Anode degradation	Diffusion process slow down
Anode half-cell	A2	–	–	A4, A5	A6
Cathode half-cell	–	–	C3, C4	–	C6
Full-cell	F2	–	F3, F4	F5	F6
Cylindrical cell	S2	S2	S3, S4	S5	S6

analyzing the full and cylindrical cells, an increase in magnitude for aged cells is found, specifically at SoH lower than 80% (IDs: FC1, REF_w/oCV, FC05). Moreover, DRT profiles at SoC = 0% and SoC = 100% of the aged cells show similar time constant shift behavior of peaks F5 and S5 compared with peak A5 of half-cells, as at BoL. Therefore, F5 and S5 attribution at BoL is confirmed (anode charge transfer phenomena) and the rise in magnitude is associated with anode degradation. 3) Peak 6: No specific trends allow to attribute peaks F6 and S6 to the anode or the cathode degradation. However, the lower the SoH, the larger the peak magnitude rise. This phenomenon can be related to general slowdown of the cells kinetic that influences diffusive processes. Consequently, this behavior confirms the attribution of F6 and S6 at BoL.

The summary of degradation mechanisms attributed to DRT peaks is given in Table 3. This analysis allowed to refine most of the attributions done already in Table 2 (e.g., the attribution of the SEI film to the second DRT peak). The tentative attribution will be validated with the results of imaging techniques that are given in the next paragraph.

3.2. Validation through Imaging

The DRT peaks attribution performed on lab and cylindrical cells (Table 2 and 3) has been validated with imaging techniques. The validation objective is twofold: 1) to address the specific degradation mechanisms occurring at anode and cathode sides and 2) to confirm that specific DRT peaks belong either to the cathode or anode electrodes. As mentioned in Section 2.3, three techniques have been exploited: digital imaging, optical microscopy, and SEM. The imaging is performed both on the graphite electrode and on the NMC electrode.

3.2.1. Graphite Electrode

After cell disassembling and unrolling, the anode looked fragile and prone to exfoliation on the edges. Digital images have been taken inside the glovebox on both electrode sides. As shown in Figure 7 for all the seven cells (NEW + aged), the most relevant deterioration is concentrated in the inner part of the electrode, that is, the area close to the positive tab. From left to right, the first two pictures represent the cell ID:NEW (100% SoH) and the cell ID:DOD20 (94% SoH): no differences or deterioration effects are detected. For all the other cells, gray film formation of variable extent is observed on the graphite surface, which can be associated with lithium plating.^[51] These visual findings have been qualitatively compared with the DRT peak variations of cylindrical cells. Table 4 assesses on a 0–5 scale the plating formation over the whole electrode surface assuming 0 for cell ID:NEW and 5 for the most plated electrode (i.e., cell ID:FC1): the larger the plated area, the larger the rise in magnitude of peak S2. In fact, deposited lithium leads to a longer path for lithium ions to intercalate into graphite and consequently blocks the contact between the electrolyte and SEI layer while reducing the available surface.^[20] The process results in an increase of resistance, which is detected by the S2 peak magnitude rise. Specifically, cell ID:FC1 reached very low SoH (63%) and shows a spotted covering on the whole graphite surface (Figure 7g). Similar effect is found in cell ID:FC05 (Figure 7e). Cell ID:REF_w/oCV instead shows a

Table 4. Trend of commercial cells' DRT peaks at 50% SoC compared with degradation detection made with digital imaging on the anode (graphite). The peak variation is small (↑) or big (↑↑) and evaluated with respect to NEW cell. Lithium plating is ranked on 0–5 scale between NEW and FC1 cells.

Cell	SoH [%]	Commercial cell DRT peaks at 50% SoC						Li plating detection with digital imaging on the anode
		S1	S2	S3	S4	S5	S6	
NEW	100	–	–	–	–	–	–	□□□□□
DOD20	94	–	↑	↑	–	–	↑	□□□□□
REF	86	–	↑	↑↑	↑	↑	↑	■□□□□
FD1	81	–	↑	↑↑	↑	↑	↑	■□□□□
FC05	79	–	↑↑	↑↑	–	↑	↑	■□□□□
REF_w/oCV	78	–	↑↑	–	–	↑	↑	■□□□□
FC1	63	↑	↑↑	–	–	↑↑	↑↑	■□□□□

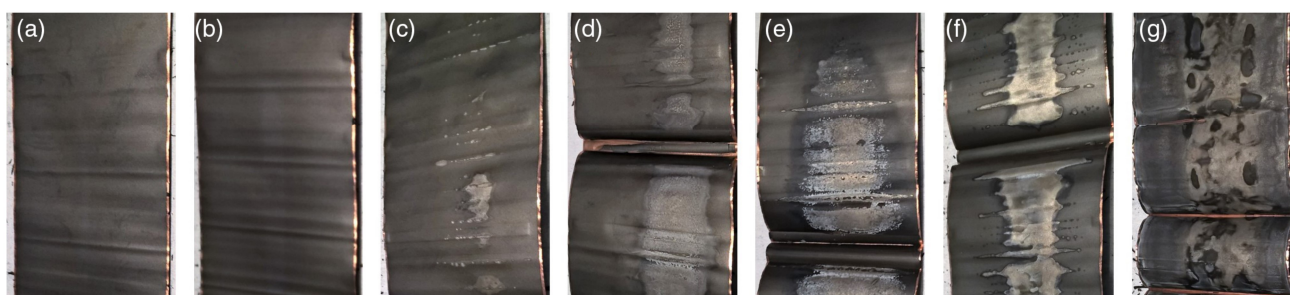


Figure 7. Digital imaging of graphite electrodes: a) NEW cell; b) DOD20 cell; c) REF cell; d) FD1 cell; e) FC05 cell; f) REF_w/oCV cell; and g) FC1 cell.

lower extension of the plated area but is shinier and more homogeneous. All the other cells, that is, ID:REF and ID:FD1 in Figure 7c,d, show a smaller plated area, corresponding to a smaller rise in magnitude of peak S2. The presence of deposited lithium on these cells suggests that lithium plating is induced by SEI layer growth and decomposition, as found in previous works.^[5,52] These analyses confirm the attribution of peak S2 to SEI layer-related phenomena and to lithium plating.

Optical microscopy has been then applied to some graphite samples, as listed in Table 1, to investigate deeper graphite degradation at the micrometer scale. **Figure 8** shows the results of optical microscopy applied to cell ID:NEW, cell ID:REF, and cell ID:FD1 both in a nonplated area and in plated one. In the first two cases (Figure 8a,b), the graphite structure is clearly visible over the whole observed area and, despite cell ID:REF reached EoT at 86% SoH; no structural changes or damages are detected if compared with pristine graphite (ID:NEW). In the case of Figure 8c, the graphite structure is visible in the background but a formation on the electrode surface hinders it partially. This formation, not visible in electrode pictures, is associated with SEI layer decomposition which led to lithium plating.

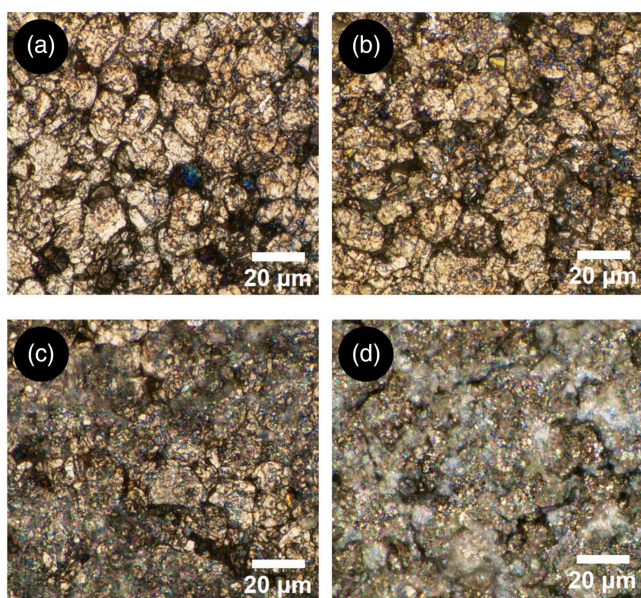


Figure 8. Optical microscope imaging of graphite electrodes: a) NEW cell; b) REF cell; c) FC1 cell in a nonplated area; and d) FC1 cell in a plated area.

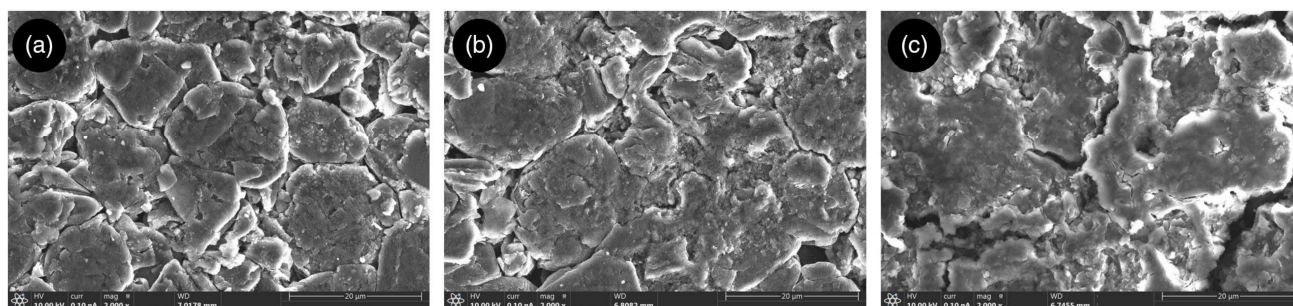


Figure 9. SEM imaging of anode electrodes: a) NEW cell; b) FC1 cell in a plated region; c) FC1 cell in a nonplated region.

When focusing on a fully plated graphite area for the same cell (Figure 8d), the graphite structure is fully covered by a layer of lithium metal with visible cracks. SEM imaging is used to investigate plated and nonplated regions when compared with the pristine sample (ID:NEW). **Figure 9b** shows cell FD1 nonplated region: graphite grains are still visible as in cell ID:NEW (Figure 9a) but partially covered with film formation. This film has cracks and irregular morphology as the one observed on the plated region of cell ID:FD1 (Figure 9c). This confirms that lithium plating, as the product of SEI layer growth, is present also when not visible with digital imaging. In general, the partial or full covering of graphite grains could inhibit the ion exchange during cell charging and discharging processes. Consequently, the presence of plating not only causes consumption of lithium ions but also loss of anode material due to its inhibition; this phenomenon is considered as graphite degradation and, in turn, affects graphite charge transfer reactions. This conclusion validates the attribution of peak S5 both at BoL and at EoL/EoT to graphite charge transfer and its degradation (Table 4).

Overall, imaging applied to the graphite electrode allowed to validate two DRT peaks: 1) peak S2, which is associated with SEI layer with its growth/decomposition degradation mechanisms and lithium plating and 2) peak S5, which with associated with graphite charge transfer reaction and graphite degradation (loss of active material).

3.2.2. NMC Electrode

Different from the graphite electrode, NMC electrodes did not show visible degradation during unrolling. The crosscomparison of all pictures taken with the digital camera showed no differences in terms of colors or surface deterioration. Therefore, more accurate investigations were performed with optical microscopy and SEM. If the first only allowed to observe the structure of NMC with its grains, or well-known “secondary particles,” the magnification from SEM provided insights on the degradation mechanisms. **Figure 10** shows the surface and cross-section SEM images of cell ID:NEW (a–d), cell ID:FC1 (b–e), and cell ID:REF (c–f). In all cases, the cathode structure with secondary particles of variable sizes is visible. Cell ID:NEW (100% SoH) and ID:FC1 (63% SoH) are quite similar in terms of particles size and material brightness. Most probably the severe fast charge protocol of cell FC1 (cell brought to EoL in less than 100 EqC) impacted only the graphite electrode, with no impact to cathode. In the case of cell ID:REF, Figure 10c shows small

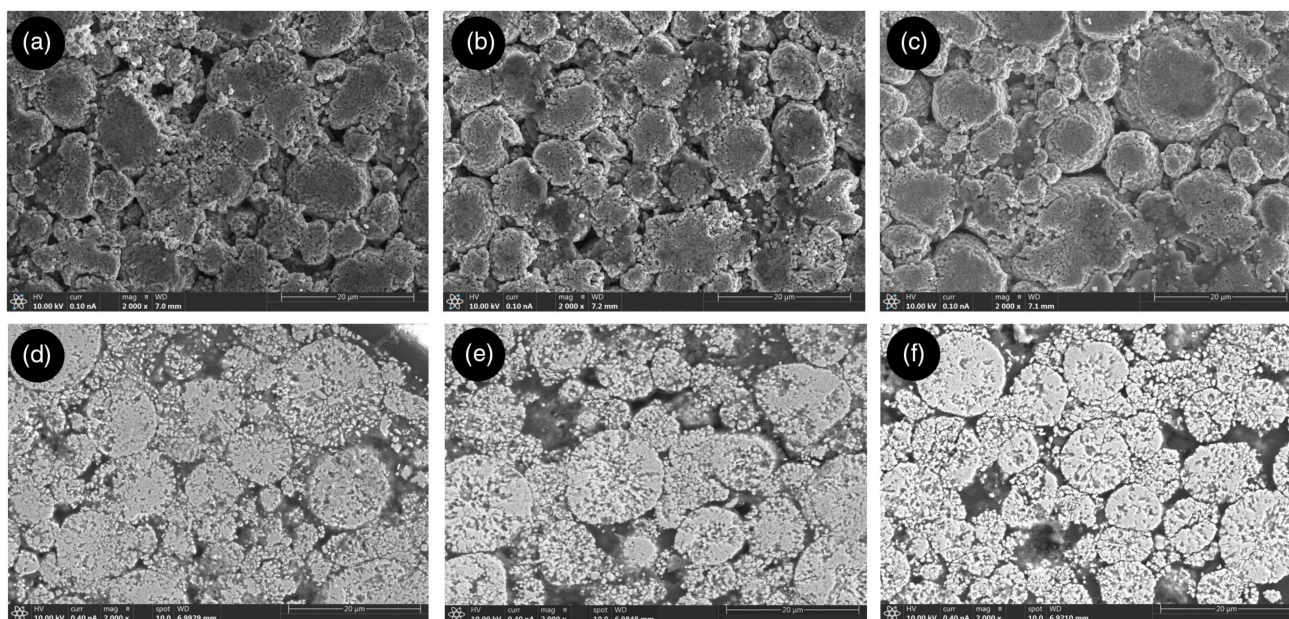


Figure 10. SEM imaging of cathode electrodes. Planar surface samples: a) new cell; b) FC1 cell; c) REF cell. Cross-section samples: d) new cell; e) FC1 cell; f) REF cell.

Table 5. Conclusive DRT peaks' attribution: physical processes and degradation mechanisms.

	DRT peaks' cylindrical cell					
	S1	S2	S3	S4	S5	S6
Time constant range [s]	$<10^{-3}$	10^{-3} – 10^{-2}	10^{-2} – 10^{-1}	10^{-1} – 10^0	10^0 – 10^1	$>10^1$
Physical process	Electric and magnetic effects	SEI	Cathode charge transfer/CEI	Cathode charge transfer	Anode charge transfer	Diffusion processes
Degradation mechanism	–	SEI growth/decomposition; Li plating	Cathode particle cracking		Graphite degradation	Kinetic slow down

cracks and a general higher shininess, which can be attributed to a higher amount of nonelectronic conductive material in the electrode, that is, to NMC degradation.^[53] Cracking is more evident, analyzing the cross-section sample in Figure 10f, where several secondary particles are affected by these degradation mechanisms compared with the cross-section samples of cells NEW and FC1 (Figure 10d,e). The differences in degradation between REF and FC1 can be related to the same difference registered in DRT peaks S3 and S4 for the same cells (Table 4). While in REF cell there is a rise in magnitude for both peaks, and this is not the case for cell ID:FC1. Therefore, it is concluded that peaks S3 and S4 can be used to track cathode degradation, mostly related to particle cracking.

3.2.3. Validation: Final Remarks

Imaging techniques allowed to validate the tentative peak attributions made at BoL (Table 2) and EoL/EoT (Table 3). The summary of physical processes and degradation mechanisms attributed to the DRT peaks of cylindrical cells is reported in Table 5, including the time constant range for each peak.

On one side, the peaks univocally attributed to the anode are S2, which accounts for SEI layer and its growth/decomposition (including lithium plating), and S5 which accounts for graphite charge transfer and its degradation. On the other side, the peaks univocally attributed to the cathode are S3 and S4, which both account for charge transfer processes and cathode particle cracking degradation. Peak S1 accounts for electric and magnetic effects and it is invariant with respect to cell degradation. Peak S6 accounts for diffusive processes and its behavior with respect to aging depends mainly by the kinetic caused in turn by the general degradation at the two electrodes.

4. Conclusion

EIS and DRT were investigated as a comprehensive measurement and a promising postprocessing method to analyze cell aging and detect the different degradation mechanisms, respectively. DRT is a powerful tool to magnify the polarization effects overlapped in the frequency domain by a peak-based

representation with different peaks (six for the tested cells) characterized by different magnitudes and time constants.

Different cycling protocols have been applied on commercial Li-ion cells to emulate different aging paths, including high charging and discharging rates and reduced DoDs. We analyzed DRT profiles at BoL and EoL/EoT and compared them for cylindrical cells and lab-made cells in coin formats (full-cells, cathode half-cells, and anode half-cells). The objectives were to discriminate between the processes at the cathode or the anode sides by analyzing the analogies between the lab-made half-cell and full-cell measurements and relate them to specific DRT peaks of commercial cells. Imaging techniques (digital imaging, optical microscopy, and SEM) on samples extracted from the cylindrical cells were used to assess the degradation mechanisms at cathode and/or anode and ultimately to validate their tentative DRT peaks attribution.

The summary of physical processes and degradation mechanisms attributed to the six DRT peaks is as follows: 1) peak S1 is invariant with respect to aging and attributed to electric and magnetic effects; 2) peak S2 is attributed to ion transport through graphite's SEI layer and it is influenced by SEI growth/decomposition and lithium plating degradation mechanisms; 3) peaks S3 and S4 are attributed to cathode charge transfer reactions and to NMC degradation due to particle cracking; 4) peak S5 is attributed to graphite's charge transfer reactions and its related graphite degradation; and 5) peak S6 is attributed to diffusive processes and accounts for general kinetic slow down due to general degradation at both electrodes.

The use of imaging techniques validated the different aging attributions at the graphite and NMC electrodes. In the first case, lithium plating was detected via digital imaging and optical microscopy and its formation from SEI layer growth/decomposition was confirmed with SEM. In the second case, only SEM imaging gave enough accuracy to appreciate particle cracking degradation on the cathode material. Therefore, it is concluded that digital imaging can be used as a validation tool to spot "macro" degradation effects on the electrode surface, while more complex tools (e.g., optical microscopy, SEM) should be used to differentiate between them and to assess their severity.

Overall, the methodology presented in this work included: 1) cell testing with different aging conditions with EIS measurements at regular intervals and cell disassembly for postmortem analyses (lab-cell making and imaging); 2) analysis of DRT profiles at BoL and EoL for peaks' attribution, comparing lab-made cells (half-cells and full-cells) with cylindrical cells; and 3) validation of the peaks' attributions through digital imaging, optical microscopy, and SEM applied on anode and cathode electrodes. All these steps can be replicated and applied to other Li-ion cells with different format sizes or cathode chemistry. However, the application of the presented methodology could be limited by two factors: 1) DRT calculation depends on the quality of EIS measurements both for commercial and for lab-made cells; therefore, it is necessary to collect reliable measurements; 2) the validation of micrometer-scale degradation mechanisms is only possible with expensive and complex techniques (such as SEM).

The findings of this work could be used to develop suitable indicators associated with DRT peaks. These indicators could be used twofold: 1) to reliably estimate the SoH, avoiding long

full-capacity measurement, and 2) to build more robust battery models (e.g., ECMs) based on parameters that are mapped from BoL to EoL.

Acknowledgements

This work was partially funded by the HIDDEN project that received funding from the European Union's Horizon 2020 research and innovation programme under grant agreement no. 957202.

Open access funding provided by Eidgenössische Technische Hochschule Zurich.

Conflict of Interest

The authors declare no conflict of interest.

Data Availability Statement

The data that support the findings of this study are available from the corresponding author upon reasonable request.

Keywords

battery aging, distribution of relaxation time, electrochemical impedance spectroscopy, imaging techniques, lithium-ion batteries, postmortem analyses

Received: May 25, 2022

Revised: August 3, 2022

Published online: August 24, 2022

- [1] J. B. Goodenough, Y. Kim, *J. Power Sources* **2011**, 196, 6688.
- [2] P. Shafiei Sabet, A. J. Warnecke, F. Meier, H. Witzhausen, E. Martinez-Laserna, D. U. Sauer, *J. Power Sources* **2020**, 449, 227369.
- [3] A. Barré, B. Deguilhem, S. Grolleau, M. Gérard, F. Suard, D. Riu, *J. Power Sources* **2013**, 241, 680.
- [4] J. Vetter, P. Novak, M. Robert Wagner, C. Veit, K.-C. Möller, J. Besenhard, M. Winter, M. Wohlfahrt-Mehrens, C. Vogler, A. Hammouche, *J. Power Sources* **2005**, 147, 269.
- [5] C. R. Birkel, M. R. Roberts, E. McTurk, P. G. Bruce, D. A. Howey, *J. Power Sources* **2017**, 341, 373.
- [6] W. Waag, C. Fleischer, D. Sauer, *J. Power Sources* **2014**, 258, 321.
- [7] C. Brivio, R. E. Carrillo, P.-J. Alet, A. Hutter, in *2020 Int. Symp. Power Electronics, Electrical Drives, Automation and Motion (SPEEDAM)*, Sorrento, Italy June 2020, pp. 184–188.
- [8] D. Andre, M. Meiler, K. Steiner, Ch Wimmer, T. Soczka-Guth, D. U. Sauer, *J. Power Sources* **2011**, 196, 5334.
- [9] C. Brivio, V. Musolino, M. Merlo, C. Ballif, *IEEE Trans. Energy Convers.* **2019**, 34, 594.
- [10] J. Illig, J. P. Schmidt, M. Weiss, A. Weber, E. Ivers-Tiffée, *J. Power Sources* **2013**, 239, 670.
- [11] C. Pastor-Fernández, K. Uddin, G. H. Chouchelamane, W. D. Widanage, J. Marco, *J. Power Sources* **2017**, 360, 301.
- [12] P. Iurilli, C. Brivio, V. Wood, *J. Power Sources* **2021**, 505, 229860.
- [13] N. Meddings, M. Heinrich, F. Overney, J.-S. Lee, V. Ruiz, E. Napolitano, S. Seitz, G. Hinds, R. Raccichini, M. Gaberšček, J. Park, *J. Power Sources* **2020**, 480, 228742.
- [14] W. Choi, H.-C. Shin, J. M. Kim, J.-Y. Choi, W.-S. Yoon, *J. Electrochem. Sci. Technol.* **2020**, 11, 14.

- [15] A. Maheshwari, M. Heck, M. Santarelli, *Electrochim. Acta*, **2018**, 273, 335.
- [16] Y. Leng, S. Ge, D. Marple, X.-G. Yang, C. Bauer, P. Lamp, C.-Y. Wang, *J. Electrochem. Soc.* **2017**, 164, A1037.
- [17] J. Bartoszek, Y.-X. Liu, J. Karczewski, S.-F. Wang, A. Mrozinski, P. Jasinski, in *2017 21st European Microelectronics and Packaging Conf. (EMPC) & Exhibition*, Warsaw September 2017, pp. 1–5.
- [18] P. Iurilli, C. Brivio, R. E. Carrillo, V. Wood, *IEEE Trans. Ind. Appl.* **2022**, 58, 1429.
- [19] B. A. Boukamp, *J. Phys. Energy* **2020**, 2, 042001.
- [20] M. Yi, F. Jiang, G. Zhao, D. Guo, D. Ren, L. Lu, M. Ouyang, in *2021 IEEE 4th Inter. Electrical and Energy Conf. (CIEEC)*, IEEE, Piscataway, NJ May 2021, pp. 1–5.
- [21] X. Zhou, J. Huang, Z. Pan, M. Ouyang, *J. Power Sources* **2019**, 426, 216.
- [22] B. Stiaszny, J. C. Ziegler, E. E. Krauß, J. P. Schmidt, E. Ivers-Tiffée, *J. Power Sources* **2014**, 251, 439.
- [23] X. Li, A. M. Colclasure, D. P. Finegan, D. Ren, Y. Shi, X. Feng, L. Cao, Y. Yang, K. Smith, *Electrochim. Acta* **2019**, 297, 1109.
- [24] L. Wildfeuer, N. Wassiliadis, A. Karger, F. Bauer, M. Lienkamp, *J. Energy Storage* **2022**, 48, 103909.
- [25] P. Shafei Sabet, G. Stahl, D. U. Sauer, *J. Power Sources* **2020**, 472, 228189.
- [26] P. Shafei Sabet, D. U. Sauer, *J. Power Sources* **2019**, 425, 121.
- [27] J. Zhou, P. H. L. Notten, *J. Power Sources* **2008**, 177, 553.
- [28] Y. Li, M. Bettge, B. Polzin, Y. Zhu, M. Balasubramanian, D. P. Abraham, *J. Electrochem. Soc.* **2013**, 160, A3006.
- [29] T. Waldmann, A. Iturrondobeitia, M. Kasper, N. Ghanbari, F. Aguesse, E. Bekaert, L. Daniel, S. Genies, I. Jiménez Gordon, M. W. Löble, E. De Vito, M. Wohlfahrt-Mehrens, *J. Electrochem. Soc.* **2016**, 163, A2149.
- [30] X. Chen, L. Li, M. Liu, T. Huang, A. Yu, *J. Power Sources* **2021**, 496, 229867.
- [31] T. P. Heins, N. Schlüter, S. T. Ernst, U. Schröder, *Energy Technol.* **2020**, 8, 1900279.
- [32] C.-H. Chen, F. B. Planella, K. O'Regan, D. Gastol, W. D. Widanage, E. Kendrick, *J. Electrochem. Soc.* **2020**, 167, 080534.
- [33] 'Product specifications - Battery Tester BCS-800 Series', <https://www.biologic.net/documents/high-throughput-battery-tester-bcs-8xx-series/> (accessed: April 2021).
- [34] Angelantoni Test Technologies, <https://www.acstestchambers.com/en/environmental-test-chambers/discovery-my-climatic-chambers-for-stress-screening/> (accessed: April 2021).
- [35] B. Manikandan, V. Ramar, C. Yap, P. Balaya, *J. Power Sources* **2017**, 361, 300.
- [36] J. Sturm, A. Rheinfeld, I. Zilberman, F. B. Spingler, S. Kosch, F. Frie, A. Jossen, *J. Power Sources* **2019**, 412, 204.
- [37] T. Waldmann, M. Kasper, M. Wohlfahrt-Mehrens, *Electrochim. Acta* **2015**, 178, 525.
- [38] J. Schmitt, M. Schindler, A. Jossen, *J. Power Sources* **2021**, 506, 230240.
- [39] N. Williard, B. Sood, M. Osterman, M. Pecht, *J. Mater. Sci.: Mater. Electron.* **2011**, 22, 1616.
- [40] H. M. Dahn, A. J. Smith, J. C. Burns, D. A. Stevens, J. R. Dahn, *J. Electrochem. Soc.* **2012**, 159, A1405.
- [41] B. A. Boukamp, *J. Electrochem. Soc.* **1995**, 142, 1885.
- [42] M. Hahn, S. Schindler, L.-C. Triebs, M. A. Danzer, *Batteries* **2019**, 5, 43.
- [43] T. H. Wan, M. Saccoccio, C. Chen, F. Ciucci, *Electrochim. Acta* **2015**, 184, 483.
- [44] S. Ma, M. Jiang, P. Tao, C. Song, J. Wu, J. Wang, T. Deng, W. Shang, *Prog. Nat. Sci.: Mater. Int.* **2018**, 28, 653.
- [45] X. Zhang, Y. Gao, B. Guo, C. Zhu, X. Zhou, L. Wang, J. Cao, *Electrochim. Acta* **2020**, 343, 136070.
- [46] E. Sarasketa-Zabala, F. Aguesse, I. Villarreal, L. M. Rodriguez-Martinez, C. M. López, P. Kubiak, *J. Phys. Chem. C* **2015**, 119, 896.
- [47] T. Yoshida, M. Takahashi, S. Morikawa, C. Ihara, H. Katsukawa, T. Shiratsuchi, J.-I. Yamaki, *J. Electrochem. Soc.* **2006**, 153, A576.
- [48] J. Li, J. Zhang, X. Zhang, C. Yang, N. Xu, B. Xia, *Electrochim. Acta* **2010**, 55, 927.
- [49] S. F. Schuster, T. Bach, E. Fleder, J. Müller, M. Brand, G. SEXTL, A. Jossen, *J. Energy Storage* **2015**, 1, 44.
- [50] M. A. Danzer, *Batteries* **2019**, 5, 53.
- [51] J. C. Burns, D. A. Stevens, J. R. Dahn, *J. Electrochem. Soc.* **2015**, 162, A959.
- [52] X.-G. Yang, Y. Leng, G. Zhang, S. Ge, C.-Y. Wang, *J. Power Sources* **2017**, 360, 28.
- [53] O. Capron, R. Gopalakrishnan, J. Jaguemont, P. Van den Bossche, N. Omar, J. Van Mierlo, *Materials* **2018**, 11, 176.